CHEMISTRY OF MATERIALS
Article

Chem. Mater. **2009,** *21,* 4223–4232 4223
DOI:10.1021/cm901757h

Detailed Phase Analysis and Crystal Structure Investigation of a $Bi_{1-x}Ca_xFeO_{3-x/2}$ Perovskite-Related Solid Solution Phase and Selected Property Measurements Thereof

Jason Schiemer,*,† Ray Withers† Lasse Norén,† Yun Liu,† Laure Bourgeois,‡ and Glen Stewart§

†*Research School Of Chemistry, Australian National University, Canberra, 0200, Australia,* ‡*Monash Centre for Electron Microscopy and Department of Materials Engineering, Monash University, V., 3800 Australia, and* §*A.D.F.A., School of Physical, Environmental & Mathematical Sciences, University of New South Wales, Canberra, ACT 2600 Australia*

Received June 24, 2009

A well-ordered, perovskite-related, $Bi_{1-x}Ca_xFe^{III}O_{3-x/2}$ solid solution phase is synthesized via a rapid liquid phase sintering technique and shown to exist over the composition range $\sim 0.20 < x < \sim 0.49$. Two phase regions are shown to separate this phase from compositionally narrow end-member $Bi_{1-x}Ca_xFe^{III}O_{3-x/2}$ solid solutions based on rhombohedral $BiFeO_3$ and brownmillerite, $Ca_2Fe_2O_5$, respectively. The wide range, non-stoichiometric phase is characterized by a well ordered, (in general) incommensurately modulated structure that varies systematically with composition. Mössbauer spectroscopy is used to verify the oxidation state of iron as (III), as well as showing the existence of three separate iron environments across the solid solution field. HRTEM imaging is used to develop a structural model for the phase at one particular composition. The magnetic, dielectric, and impedance properties of this solid solution phase are reported. Magnetic measurements show antiferromagnetic behavior. There is no change in either susceptibility or antiferromagnetic behavior with composition. Attempts at obtaining saturated ferroelectric loops failed due to high intrinsic conductivity. The phase is found to exhibit a low frequency impedance relaxation that is likely due to correlated oxygen vacancy hopping.

Introduction

High performance, lead-free ferroelectric materials are widely sought to replace lead-based ferroelectric materials (such as PZT) in devices such as piezoelectric actuators or ferroelectric electronic devices such as FRAM. Such replacement materials would have obvious benefits over their lead-based analogues through lower health and environmental impact in manufacturing, use, and disposal. One such lead-free, ferroelectric material, $BiFeO_3$ (BFO), holds additional interest due to the fact that it is also magnetically active. BFO's dual ferroelectric and ferromagnetic activity place it into the class of multiferroic materials. BFO is one of the few multiferroic materials that can function at room and elevated temperatures (with a Neél temperature of 640 K and a Curie temperature of 1100 K). This makes it particularly attractive for device applications.

The measurement of a ferroelectric hysteresis loop in BFO itself has proven rather difficult as a result of high leakage currents. Various proposals have been put forward as to the mechanism of conduction, including the presence of Fe^{II} and/or oxygen vacancies or small levels of impurity phase.[1] While Mössbauer spectroscopy[2] shows that very little, if any, Fe^{II} exists in bulk ceramic BFO, large amounts of Fe^{II} (up to 50%) have been reported in thin films of BFO using X-ray photoelectron spectroscopy.[3] Various groups have managed to suppress conduction in bulk ceramic BFO either via quenching, low temperature synthesis, or high pressure synthesis. The latter high pressure approach, for example, led to a remnant polarization of 46 $\mu C/cm^2$ and a coercive field of 73 kV/cm,[4] on par with the best thin film results which have reported remnant polarizations in excess of 110 $\mu C/cm^2$, though with impractically large coercive fields $\sim$ 400 kV/cm.[5]

The desire to improve the magnetic and ferroic properties of pure BFO has lead to widespread interest in $BiFeO_3$-doped materials. Doping with large alkaline earth ions on the perovskite A site, for example, has been shown to disrupt the spin cycloid and change the material into a weak ferromagnet.[6] Doping with Sr^{2+} and Ca^{2+}

(1) Zhang, S. T.; Lu, M. H.; Wu, D.; Chen, Y. F.; Ming, N. B. *Appl. Phys. Lett.* **2005**, *87*(26), 262907-3.
(2) Lebeugle, D.; Colson, D.; Forget, A.; Viret, M.; Bonville, P.; Marucco, J. F.; Fusil, S. *Phys. Rev. B* **2007**, *76*, 024116.
(3) Wang, Y.; Jiang, Q.-h.; He, H.-c.; Nan, C.-W. *Appl. Phys. Lett.* **2006**, *88*(14), 142503-3.
(4) Su, W. N.; Wang, D. H.; Cao, Q. Q.; Han, Z. D.; Yin, J.; Zhang, J. R.; Du, Y. W. *Appl. Phys. Lett.* **2007**, *91*(9), 092905–3.
(5) Yun, K. Y.; Ricinschi, D.; Kanashima, T.; Okuyama, M. *Appl. Phys. Lett.* **2006**, *89*(19), 192902-3.
(6) Khomchenko, V. A.; Kiselev, D. A.; Selezneva, E. K.; Vieira, J. M.; Lopes, A. M. L.; Pogorelov, Y. G.; Araujo, J. P.; Kholkin, A. L. *Mater. Lett.* **2008**, *62*(12−13), 1927–1929.

Published on Web 08/24/2009

ions, on the other hand, gives rise to a poorly understood $Bi_{1-x}M_xFeO_{3-x/2}$ phase.[7,8] Under a large magnetic field (~5−10 T),[9] one member of this phase has been reported to exhibit a very large polarization (96 $\mu C/cm^2$) and a very low coercive field (661 V/cm).

In this paper, a careful synthesis, phase analysis and crystal structure investigation is made of a wide range, non-stoichiometric solid solution phase within the $Bi_{(1-x)}Ca_xFeO_{(3-x/2)}$ (BCFO) system. Room temperature magnetic properties are investigated, as well as the ferroelectric, dielectric, and resistivity properties at selected compositions. The oxidation state, as well as the local co-ordination environments, of Fe are carefully investigated via ^{57}Fe Mössbauer spectroscopy. The examination builds on the recent investigations of BCFO reported by Troyanchuk et al.[10] and Chen et al.[11] HRTEM imaging is used to develop a structural model for the phase at one paticular composition.

Experimental Procedure

Synthesis. Samples of nominal composition $Bi_{1-x}Ca_xFeO_{3-x/2}$ (BCFO) from $x = 0.1-0.75$ were prepared by a rapid two-stage reaction method using high purity Bi_2O_3, $CaCO_3$, and Fe_2O_3 powders following the work by Khomchenko et al.[12] The liquid phase of Bi_2O_3 was utilized to yield surprisingly short reaction times but nonetheless extremely well-crystallized reaction products. The starting powders were first homogenized for ~20 min in an agate mortar before initial reaction at 850 °C for 20 min. The resultant samples were then reground for a further 20 min, pressed into a pellet at 480 MPa in a steel die, and sintered according to composition. Samples with $x < 0.3$ were sintered at 940 °C for 20 min, while samples with $x > 0.3$ were sintered at 990 °C for 20 min. Use of sintering temperatures much above these caused melting of the samples. Compositions were prepared from $x = 0.1$ to 0.75 to examine the composition range of a suspected continuous $Bi_{1-x}Ca_xFeO_{3-x/2}$ solid solution and any adjacent two phase regions neighboring it in the overall composition range investigated.

Little to no loss of bismuth was observed during the reaction process for all samples, both by measurement of weight change after reaction and from subsequent electron microprobe analysis in the SEM. For this reason, all mixtures were prepared with stoichiometric ratios of starting reagents. Any possible surface effects were addressed by an aggressive polishing scheme, which removed the outer surface layers.

X-ray Diffraction. X-ray powder diffraction work was performed with a Guinier-Hägg camera using monochromatic Cu $K\alpha_1$ radiation. Pure silicon (Sietronics GD#1[13]) was added as an internal standard and the software package "Unitcell"[14] used for accurate determination of the resultant unit cell parameters.

SEM Characterization. To check for homogeneity as well as to establish the resultant compositions, the samples were also quantitatively analyzed via electron probe micro-analysis (EPMA) using a JEOL 6400 SEM with an Oxford ISIS EDXA detector (operating conditions: 15 kV, 1 nA, 39 mm working distance). Bi_2O_3, Fe_2O_3, and diopside were used as calibration standards. Imaging was performed on this JEOL 6400 SEM as well as on a Zeiss UltraPlus analytical FESEM.

Transmission Electron Microscopy. Electron diffraction patterns (EDPs) were obtained using a Philips EM 430 transmission electron microscope (TEM) operating at 300 kV on crushed sample powders dispersed onto holey carbon coated, copper grids. High resolution (HR)TEM images were collected on a JEOL 2100F TEM operating at 200 kV and with Scherzer defocus = −61 nm on the same crushed samples. HRTEM simulations were performed via the multi-slice method[15] using the JEMS software package.[16]

Mössbauer Spectroscopy. ^{57}Fe−Mössbauer spectroscopy was used to investigate the oxidation state of Fe in the samples as well as to investigate the number of distinct local environments around the Fe cations throughout the solid solution field. Mössbauer spectra were recorded at room temperature with a ^{57}Co:Rh source mounted on a drive having sinusoidal motion. The 2.5 cm^2 absorbers consisted of 80 mg of specimen diluted with 100 mg of CB4 filler. The maximum drive velocity was calibrated against the standard spectrum of an α-Fe foil.

Electrical Characterization. To carry out electrical characterization, selected pellets were coated with silver paste on each side and then heat treated at 500 °C for 30 min to ensure good electrical contact. Dielectric properties were collected on a high precision LCR meter (Agilent 4284A), while ferroelectric hysteresis measurements were carried out on an aixACCT TF 2000 FE analyzer. Resistance measurements were carried out using a METEX 3850D multimeter.

Magnetic Property Measurements. For each specimen, the room temperature magnetization was recorded as a function of increasing and decreasing magnetic field (to a maximum field of 14 kG) using a conventional PAR vibrating sample magnetometer. The measurements were calibrated against the known magnetization of high purity nickel at 10 kG.

Results and Discussion

Synthesis. During initial syntheses, it was noted that there was a consistent slow upward trend in melting point of the intermediate product with increasing Ca content. The second heat treatment for the low calcium content samples ($x \leq 0.30$) was thus set to a slightly lower temperature of 940 °C than that set by Khomchenko et. al.[12] while that for the high calcium content samples ($x > 0.30$) was set to 990 °C, as per Khomchenko et. al.[12] For compositions within the continuous $Bi_{1-x}Ca_xFe^{III}O_{3-x/2}$, $\sim 0.2 < x < \sim 0.49$, solid solution region, ordering occurred readily within the 20 min heat treatment at the

(7) Withers, R. L.; Bourgeois, L.; Balamurugan, K.; Harish Kumar, N.; Santhosh, P. N.; Woodward, P. M. A TEM investigation of the $(Bi_{1-x}Sr_x)Fe^{3+}O_{3-x/2}$, $0.2 \leq x \leq 0.67$, solid solution and a suggested superspace structural description thereof. *J. Solid State Chem.* **2009**, *182*, 2176–2184.
(8) Lepoittevin, C.; Malo, S.; Barrier, N.; Nguyen, N.; Van Tendeloo, G.; Hervieu, M. *J. Solid State Chem.* **2008**, *181*(10), 2601–2609.
(9) Kundys, B.; Maignan, A.; Martin, C.; Nguyen, N.; Simon, C. *Appl. Phys. Lett.* **2008**, *92*(11), 112905–3.
(10) Troyanchuk, I.; Karpinsky, D.; Bushinskii, M.; Prokhnenko, O.; Kopcevicz, M.; Szymczak, R.; Pietosa, J. *J. Exp. Theor. Phys.* **2008**, *107*(1), 83–89.
(11) Chen, W.-t.; Williams, A. J.; Ortega-San-Martin, L.; Li, M.; Sinclair, D. C.; Zhou, W.; Attfield, J. P. *Chem. Mater.* **2009**, *21* (10), 2085–2093.
(12) Khomchenko, V. A.; Kiselev, D. A.; Vieira, J. M.; Jian, L.; Kholkin, A. L.; Lopes, A. M. L.; Pogorelov, Y. G.; Araujo, J. P.; Maglione, M. *J. Appl. Phys.* **2008**, *103*(2), 024105-6.
(13) Sietronics Pty Ltd. In Unit 3/22 Walder Street Belconnen, ACT 2612, Australia.
(14) Noläng, B. *Unitcell*; Ben Systems: Örnsätra, Sweden, 1990.
(15) Cowley, J. M.; Moodie, A. F. *Acta Crystallogr.* **1957**, *10*(10), 609–619.
(16) Stadelmann, P. *EMS Java Version*, CIME-EPFL: Lausanne, Switzerland, 1999.

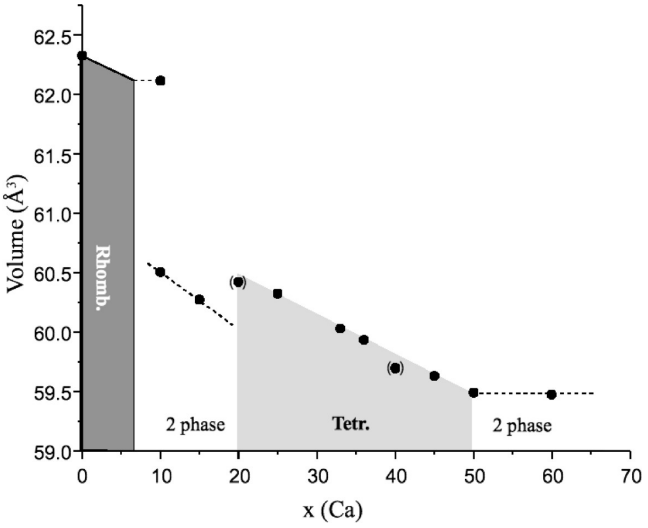

Figure 1. Shows unit cell volumes (in cubic Ångströms) with composition (x) for the $Bi_{1-x}Ca_xFeO_{3-x/2}$, $0.1 \leq x \leq 0.6$, samples based on refined powder diffraction data. Single phase regions are shown in light grey (metrically tetragonal) or dark grey (rhombohedral). Data points placed within brackets are from samples that had not completely reached equilibrium.

maximum temperature for the given compositions. (Note that ordering in this context was judged primarily by the appearance of sharp satellite reflections characteristic of the $Bi_{1-x}Ca_xFeO_{3-x/2}$ solid solution[7,8] in electron diffraction patterns (EDPs) but was not apparent in the XRD patterns.) The resultant densities, however, were found to be rather poor for most samples during initial runs with standard reagents. A new Fe_2O_3 powder with a particle size $< 5\,\mu$m (99+%, Aldrich) was thus used. With the use of this reagent, the resultant sample densities increased significantly to ~93%, sufficient for electrical characterization. As $CaCO_3$ breaks down to CaO while Bi_2O_3 melts during the initial reaction step, it was not entirely unexpected that the particle size of the Fe_2O_3 reagent should play an important role in the resultant sample density.

X-ray Diffraction. Careful analysis of the Guinier-Hägg X-ray powder diffraction (XRD) patterns was utilized to look for the presence or otherwise of minor phases, particularly near the expected two-phase regions at either end of the $Bi_{1-x}Ca_xFe^{III}O_{3-x/2}$ solid solution composition range, as well as to examine the variation in average structure metric symmetry and unit cell dimensions within the solid solution range itself (see Figure 1 and Table 1).

The expected $Bi_{1-x}Ca_xFe^{III}O_{3-x/2}$ solid solution phase was found to exist from $\sim 0.20 < x < \sim 0.49$, as judged by the appearance of sharp satellite reflections characteristic of the $Bi_{1-x}Ca_xFeO_{3-x/2}$ solid solution phase in EDPs[7,8] but also by the variation in average structure unit cell volume of this phase with nominal composition (as shown in Figure 1). Note that an essentially linear contraction of the average structure unit cell volume with increasing Ca content is observed in this region in line with expectations from Vegard's law.[17] Note that the $x = 0.4$ and 0.2 sample points are placed within brackets in Figure 1 as the former sample contained detectable traces of brownmillerite ($Ca_2Fe_2O_5$) and Fe_2O_3 likely caused by the reaction not having quite reached equilibrium, while the latter shows hints of the β-solid solution reported by Yang et al.[18] as well as the solid solution studied. The presence of this β-phase yields a slightly anomalous unit cell volume for the $x = 0.2$ sample, due to a superposition of the diffraction lines from both phases, leading to an unnatural line broadening with a trend to lower unit cell volume.

(17) Vegard, L. *Z. Phys. Hadrons Nuclei* **1921**, *5*(1), 17–26.

Table 1. Unit Cell Parameters of $Bi_{(1-x)}Ca_xFeO_{(3-x/2)}$ in Ångström (Å) Units Refined from Guinier-Hägg Powder Diffraction Data[a]

x	a	c	V	α
0	3.965(1)	*	62.326	89.45(5)
0.1	3.9605(4)	*	62.116(12)	89.479(10)
0.1	3.9258(6)	*	60.502(29)	90
0.15	3.9208(3)	*	60.273(13)	90
0.2	3.9228(3)	3.9262(5)	60.420(12)	90
0.25	3.9212(2)	3.9231(2)	60.322(6)	90
0.33	3.9150(2)	3.9164(3)	60.027(8)	90
0.36	3.9121(3)	3.9160(4)	59.933(10)	90
0.4	3.9065(3)	3.9116(5)	59.694(12)	90
0.45	3.9036(4)	3.9131(6)	59.629(16)	90
0.5	3.8999(5)	3.9112(6)	59.487(16)	90
0.6	3.8965(10)	3.9169(12)	59.47(3)	90

[a] The data for the end member $BiFeO_3$ is taken from Kubel et al.[19]

The $x = 0.2$ sample was almost completely single phase (with only ~1−2% Fe_2O_3 impurity) to XRD, while the $x = 0.25$ sample was completely free from contamination. The $x = 0.15$ sample seems to be predominantly the β-phase, while containing hints of the rhombohedral and the studied parent solid solution, suggesting that the lower limit for Ca content of the solid solution phase is at $x \sim 0.20$. At the other end of the solid solution, the nominally $x = 0.5$ sample, while predominantly belonging to the $Bi_{1-x}Ca_xFeO_{3-x/2}$ solid solution phase, nonetheless also contained a small amount of an initially unidentified second phase. By the $x = 0.75$ composition, the amount of this second phase had grown sufficiently that it could be unequivocally identified as brownmillerite, $Ca_2Fe_2O_5$. Note that this experimental observation is consistent with the following disproportionation relation

$$2Bi_{0.25}Ca_{0.75}Fe^{III}O_{2.625}\ (x = 0.7) \rightarrow$$
$$1Bi_{0.50}Ca_{0.50}Fe^{III}O_{2.75}\ (x = 0.50)$$
$$+\frac{1}{2}Ca_2Fe_2O_5\ (\text{brownmillerite})$$

The presence of a minor amount of the brownmillerite phase in the $x = 0.5$ sample suggests that the upper limit for Ca content in the solid solution is slightly less than 0.5, at $x \sim 0.49$.

The $x = 0.1$ sample clearly contained two independent perovskite-related phases, a metrically cubic phase and a

(18) Yang, C. H.; Seidel, J.; Kim, S. Y.; Rossen, P. B.; Yu, P.; Gajek, M.; Chu, Y. H.; Martin, L. W.; Holcomb, M. B.; He, Q.; Maksymovych, P.; Balke, N.; Kalinin, S. V.; Baddorf, A. P.; Basu, S. R.; Scullin, M. L.; Ramesh, R., Electric modulation of conduction in multiferroic Ca-doped $BiFeO_3$ films. *Nat. Mater.*, **2009**, *8*, 485–493.

phase of rhombohedral metric symmetry with a distinctly increased volume (see Table 1). The volume of this metrically rhombohedral phase in the $x = 0.1$ sample was 62.12 Å^3, slightly lower than the reported volume for $BiFeO_3$ itself of 62.30 Å^3,[19] consistent with a small amount of Ca substituting for Bi. We thus identify this metrically rhombohedral phase with a rather narrow $Bi_{1-x}Ca_xFe^{III}O_{3-x/2}$, $0 \leq x \leq \sim 0.07$, solid solution based on the end-member $BiFeO_3$. Electron diffraction investigation of the $x = 0.1$ and $x = 0.15$ samples (see below) confirms the existence of such a $Bi_{1-x}Ca_xFe^{III}O_{3-x/2}$, $0 \leq x \leq \sim 0.07$, solid solution but also of additional unidentified phases (see below) suggesting that kinetic considerations may be coming into play in this part of the composition range. At the other end of the phase diagram, the volume of the end-member brownmillerite ($Ca_2Fe_2O_5$) phase was slightly larger than that of pure $Ca_2Fe_2O_5$ itself, suggesting the substitution of a small amount of Bi for Ca in this end-member phase.

XRD showed the average structure of the wide range non-stoichiometric $Bi_{1-x}Ca_xFe^{III}O_{3-x/2}$, $\sim 0.2 < x < \sim 0.49$, solid solution phase to be very close to metrically cubic over most of the observed composition range (see Table 1) except towards the high Ca content end. The metric symmetry of the end-member $x \sim 0.49$ composition, for example, was clearly tetragonal rather than cubic (see Table 1). Close re-inspection of the lower Ca content XRD patterns, even the $x = 0.2$ sample, showed slight broadening of all the reflections that are split in the $x = 0.5$ sample (but not the *hhh*-type reflections) suggesting that the true metric symmetry across the whole solid solution field is in fact tetragonal, although close to metrically cubic.

Mössbauer Spectroscopy. The room temperature ^{57}Fe−Mössbauer spectra are shown in Figure 2 for BCFO specimens with composition x ranging from 0.2 to 0.5. The spectrum for $x = 0.2$ is well described by the superposition of three distinct magnetically split sextets. The most intense of the three sextets (with 72.1% of the total absorption intensity) was fitted using a magnetic hyperfine field of $B_{hf}(I) = 49.9$ T and an isomer shift $\delta(I) = 0.39$ mm/s relative to α-Fe. The equivalent parameters fitted to the second sextet are $B_{hf}(II) = 48.3$ T and $\delta(II) = 0.39$ mm/s. These results are consistent with high-spin Fe^{3+}.

In all other spectra, these two sextets are fitted slightly differently. The first (or dominant) subspectrum is fitted with essentially the same parameters, that is, $B_{hf}(I) = 49.6$ T and $\delta(I) = 0.39$ mm/s. The second sextet, however, has been fitted with slightly different parameters, namely, $B_{hf}(I) = 46.1$ T and $\delta(I) = 0.48$ mm/s. Note that the intensity associated with the second sextet drops from 24.6 % for $x = 0.2$ to 7.9% for $x = 0.25$ and then steadily climbs to 9.3% for $x = 0.4$. This may indicate that the second sextet in the 0.2 sample is primarily a line shape modifier. As a result of the low calcium content in the 0.2 sample, the second sextet observed in the other four

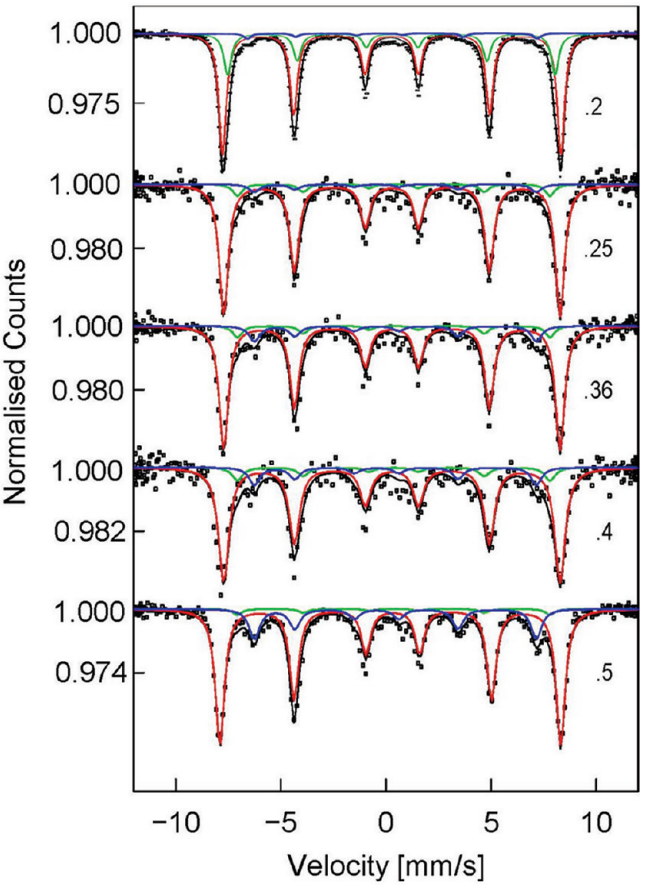

Figure 2. ^{57}Fe−Mössbauer spectra of BCFO, $x = 0.2$, 0.25, 0.36, 0.4, and 0.5, samples. The fitted theoretical curves are a superposition of three magnetically split sextets associated with a dominant octahedral site (the red line), a possible square pyramidal site (the green line), and a possible tetrahedral site (the blue line).

samples may be obscured. The results from the $x = 0.25-0.5$ samples are in close agreement with those reported recently for $Bi_{0.8}Pb_{0.2}FeO_3$[20] and are consistent with high-spin Fe^{3+}. It is believed that the less intense sextet is associated with Fe^{3+} ions located in sites of square pyramidal (or tetrahedral) coordination.

In all spectra there is clear evidence for a third magnetically split sextet (in blue) which was fitted using $B_{hf}(III) = 42.7$ T, $\delta(III) = 0.11$ mm/s, and a non-zero quadrupole interaction of $^1/_2eQV_{zz} = 0.6$ mm/s. The intensity of this sextet is largest in the $x = 0.5$ sample. This increase is most likely due to an additional contribution from the brownmillerite ($Ca_2Fe_2O_5$) impurity phase in the $x = 0.5$ sample. The spectrum of brownmillerite ($Ca_2Fe_2O_5$) is reported to be made up of two magnetically split sextets of equal intensity.[21] The absorption line

(19) Kubel, F.; Schmid, H. *Acta Crystallogr., Sect. B* **1990**, *46*(6), 698–702.

(20) Khomchenko, V. A.; Kiselev, D. A.; Kopcewicz, M.; Maglione, M.; Shvartsman, V. V.; Borisov, P.; Kleemann, W.; Lopes, A. M. L.; Pogorelov, Y. G.; Araujo, J. P.; Rubinger, R. M.; Sobolev, N. A.; Vieira, J. M.; Kholkin, A. L. Doping strategies for increased performance in $BiFeO_3$. *J. Magn. Magn. Mater.* **2009**, *312* (11), 1689–1808.

(21) Redhammer, G. J.; Amthauer, G.; Tippelt, G.; Lottermoser, W.; Roth, G. ^{57}Fe Mossbauer Spectroscopic Investigations on the Brownmillerite Series $Ca_2(Fe_{(2-x)}Al_xO_5$. *Proceedings of Industrial Applications of the Mossbauer Effect: International Symposium on the Industrial Applications of the Mossbauer Effect*, Madrid, Spain, 2005; AIP: Madrid, Spain, 2005; pp 179−184.

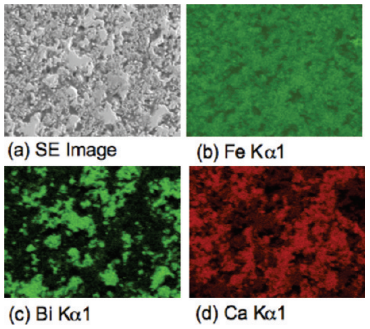

Figure 3. (a) Secondary electron (SE) image of the BCFO, $x = 0.75$, sample. (b) X-ray map of Fe $K\alpha_1$, (c) X-ray map of Bi $K\alpha_1$, and (d) X-ray map of Ca $K\alpha_1$.

positions of one of these are close to what we require and those of the second sextet would contribute to the shape complexity of the dominant BCFO sextet's absorption lines. This sub-spectrum increases from 3.3% intensity for $x = 0.2$ to 12.5% for $x = 0.4$, with a jump to 19.9% for $x = 0.5$. The spectrum has a somewhat ambiguous isomer shift (0.11 mm/s). The B_{hf} of 42.7 T, however, is inconsistent with most studies of Fe^{IV}, which indicate a B_{hf} of between 18 and 35 T.[22] It is, however, consistent with Fe^{III}. This observation, combined with the presence of a similar spectrum in brownmillerite, suggests that the signal also arises from Fe^{III}.

According to the present spectral analysis, the proportion of the blue minority environment sextet grows slowly with x, with a sharp increase between $x = 0.4$ and $x = 0.5$. Since brownmillerite has half iron octahedra and half iron tetrahedra, we thus identify this minority environment sextet with tetrahedrally coordinated Fe. The existence of this sextet strongly suggests that there must be three distinct Fe^{III} environments in BCFO. The existence of Fe^{III} in all samples contrasts with a number of thin film investigations of BFO, which found up to 56% Fe^{II}-ions through use of X-ray photoelectron spectroscopy[3] and confirms the provisional stoichiometry of $Bi_{1-x}Ca_xFe^{III}O_{3-x/2}$. This information is in disagreement with the interpretation in terms of Fe^{IV} cations suggested in a recent paper on this same solid solution.[11]

SEM Characterization—EPMA. The average composition of all samples, as found by quantitative electron probe microanalysis (EPMA), was the same as the nominal composition in each case within a 1−2% error margin; that is, no variation of stoichiometry as a result of bismuth evaporation could be detected. Electron backscattered imaging showed very slight mottling in all samples suggesting some slight inhomogeneous mixing on the local scale. For the most part, however, local composition varied by less than 1% throughout given areas of any particular sample. This reinforces the impression obtained from XRD of well crystallized single-phase samples across the entire $Bi_{(1-x)}Ca_xFe^{III}O_{(3-x/2)}$, $\sim 0.2 < x < \sim 0.49$, solid solution composition range.

(22) Adler, P. *Phys. Rev. B: Condens. Matter Mater. Phys.* **2008**, *77*(13), 136401-1.

By contrast, outside the solid solution composition range, the $x = 0.1$ sample was heavily mottled on a relatively small scale ($< 2\ \mu m$) making it difficult to get reliable EPMA readings of the composition of the individual constituent phases. The $x = 0.6$ and 0.75 samples likewise clearly showed two distinct co-existing phases, found by EPMA to be brownmillerite ($Ca_2Fe_2O_5$) with slight Bi incorporation and the $Bi_{(1-x)}Ca_xFe^{III}O_{(3-x/2)}$ solid solution phase at $x \sim 0.5$. The $x = 0.75$ sample can clearly be seen as two phase from the SEM image shown in Figure 3a. This figure also shows elemental maps b−d giving an intuitive picture of the location of the BCFO and brownmillerite phases.

Transmission Electron Microscopy (TEM). Electron diffraction patterns (EDPs) of the $Bi_{(1-x)}Ca_xFe^{III}O_{(3-x/2)}$, $\sim 0.2 \leq x \sim 0.49$, solid solution phase samples exhibited essentially the same composition-dependent, (3+1)-D modulated structure previously identified in the analogous Sr substituted bismuth ferrite system (BSFO).[7,8] In addition to the set of strong Bragg reflections of the underlying perovskite-related parent structure, labelled **G** hereafter, there are a host of (in general, incommensurate) satellite reflections characterized by the composition-dependent, primary modulation wave-vector $\mathbf{q}_{prim} = {}^1/_2\mathbf{b}_p^* + \gamma\mathbf{c}_p^*$ (with $\gamma \sim 0.37-0.42$, see the reflection labelled 0101 in Figure 4d). In addition to these $\mathbf{G} \pm m\mathbf{q}_{prim}$ satellite reflections, $\mathbf{G} \pm {}^1/_2[110]_p^*$ Bragg reflections (arrowed but not labelled in Figure 4 a,d) are also, in general, present. Indexation in Figure 4 is thus with respect to the (3+1)-D recipocal lattice basis set $M^* = \{{}^1/_2\mathbf{a}_p^*, {}^1/_2\mathbf{b}_p^*, \mathbf{c}_p^*, \mathbf{q} = \gamma\mathbf{c}_p^*\}$.

The (in general, incommensurate) satellite reflections arise from O/□ (□ an oxygen vacancy) and Bi/Ca ordering and associated structural relaxation.[7,8] Figure 4(a−d), for example, shows typical $\langle 001\rangle_p$ (subscript p for parent perovskite sub-structure) type zone axis EDPs with γ values of (a) 0.386(1), (b) 0.400(1), (c) 0.417(1), and (d) 0.375(1) found in $x = 0.333$, 0.20, 0.25, and 0.375 samples, respectively. While there were minor differences in the measured value of γ observed from grain to grain in most samples, this variation was usually quite small. It presumably arises due to diffusion limitations arising from the short reaction time used. The observed systematic linear decrease in average γ value with composition, x, is shown plotted against x in Figure 5.

Given the very close to cubic metric symmetry throughout the solid solution composition range (see Table 1), it is hardly surprising that twinning of this (3+1)-D modulated structure is very common. Thus one or more of the six (originally symmetry-equivalent) primitive primary modulation wave-vectors ($[0,{}^1/_2,\gamma]^*$, $[{}^1/_2,0,\gamma]^*$, $[\gamma,0,{}^1/_2]^*$, $[\gamma,{}^1/_2,0]^*$, $[{}^1/_2,\gamma,0]^*$, or $[0,\gamma,{}^1/_2]^*$) are often simultaneously present in EDPs as, for example, in the case of the EDPs shown in Figure 4a−c where the incommensurate component of the primitive primary modulation wave-vector appears to run along different parent perovskite $\langle 001\rangle_p^*$ directions simultaneously as a result of twinning. Occasionally, however, it is possible to obtain an apparently single domain EDP where the incommensurate component of the primitive primary modulation wave-vector

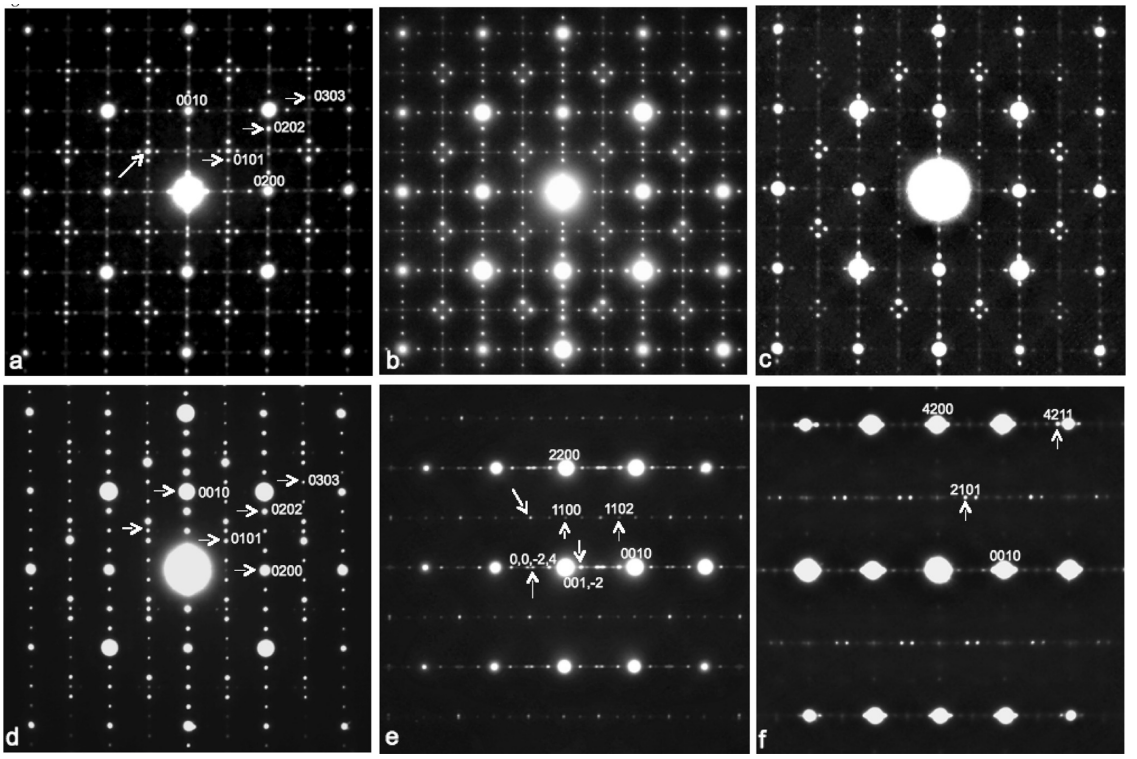

Figure 4. (a−d) Typical $\langle 001 \rangle_p$ (subscript p for parent perovskite sub-structure) type zone axis EDPs with γ values of (a) 0.386(1), (b) 0.400(1), (c) 0.417(1), and (d) 0.375(1) found in $x = 0.333$, 0.20, 0.25, and 0.375 samples, respectively. (e) Typical $\langle -1,1,0 \rangle_p$ zone axis EDP of an $x = 0.333$ sample with $\gamma = 0.386(1)$ and (f) typical $\langle -1,2,0 \rangle_p$ zone axis EDP of an $x = 0.2$ sample with $\gamma = 0.417(1)$. Indexation in all cases is with respect to the (3+1)-D recipocal lattice basis set $\mathbf{M}^* = \{^1/_2\mathbf{a}_p^*, {}^1/_2\mathbf{b}_p^*, \mathbf{c}_p^*, \mathbf{q} = \gamma\mathbf{c}_p^*\}$.

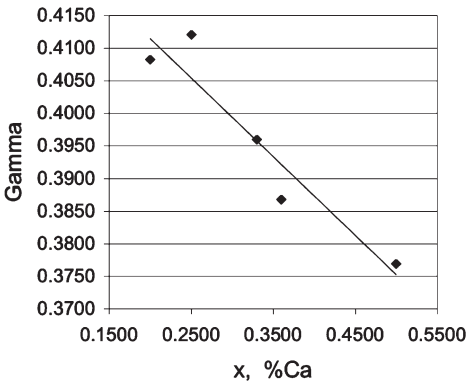

Figure 5. Shows the measured variation of γ with composition x across the $Bi_{1-x}Ca_xFeO_{3-x/2}$, $\sim 0.2 < x < \sim 0.49$, solid solution field.

only runs parallel to one of the parent perovskite $\langle 001 \rangle_p^*$ directions (see, e.g., Figure 4d). In the case of the analogous BSFO solid solution phase, this was usually not possible as the nano-scale of this form of twinning was much less than the minimum illuminated area in selected area electron diffraction.[4] HRTEM images confirm, in the current case of BCFO, that there exist relatively large areas in which the incommensurate component of the primitive primary modulation wave-vector runs along the same direction (see, e.g., Figure 6).

Note, however, that there is a rather more subtle form of twinning involving twin domains characterized by primitive primary modulation wave-vectors which have the same incommensurate reciprocal lattice direction but differ in the accompanying rational wave-vector component (e.g., $[0,{}^1/_2,\gamma]^*$ and $[{}^1/_2,0,\gamma]^*$). Figure 6, for example, shows a typical HRTEM image of a $\gamma = 0.40$ grain viewed near Scherzer defocus. [010]- and [100]-type domains typically 10−30 nm wide are visible. The insets in Figure 6 show enlargements of these [010] and [100] twin domains, along with corresponding image simulations and structure model, which will be discussed below. Note the expected 5**x** repeat along the parent $\mathbf{c}_p$ direction on both the left and right hand sides of the image. On the right hand side of the image, corresponding to a [100] orientation, the repeat along the orthogonal $\mathbf{b}_p$ direction is clearly doubled, but this is not the case on the left hand side of the image which thus corresponds to an [010] orientation. This rather more subtle form of twinning typically occurs on a finer scale than the more obvious form of twinning discussed in the immediately preceding paragraph making it virtually impossible to obtain true single domain selected area EDPs. Nonetheless, it is possible with careful positioning of an incident convergent probe to obtain very close to single domain convergent beam electron diffraction (CBED) patterns as shown in the (a) [100], (b) [010], and (c) [001] convergent beam patterns (CBPs) shown in Figure 7 using a 2 nm diameter focused probe. Indexation in Figure 7 is again with respect to the (3+1)-D reciprocal lattice basis vector set $\mathbf{M}^* = \{^1/_2\mathbf{a}_p^*, {}^1/_2\mathbf{b}_p^*, \mathbf{c}_p^*, \mathbf{q} = \gamma\mathbf{c}_p^*\}$. Note that a trace of twinning is still apparent in Figure 7b (see the arrowed reflection).

It is notable that when made under the same synthesis conditions, the satellite reflections of the BSFO samples

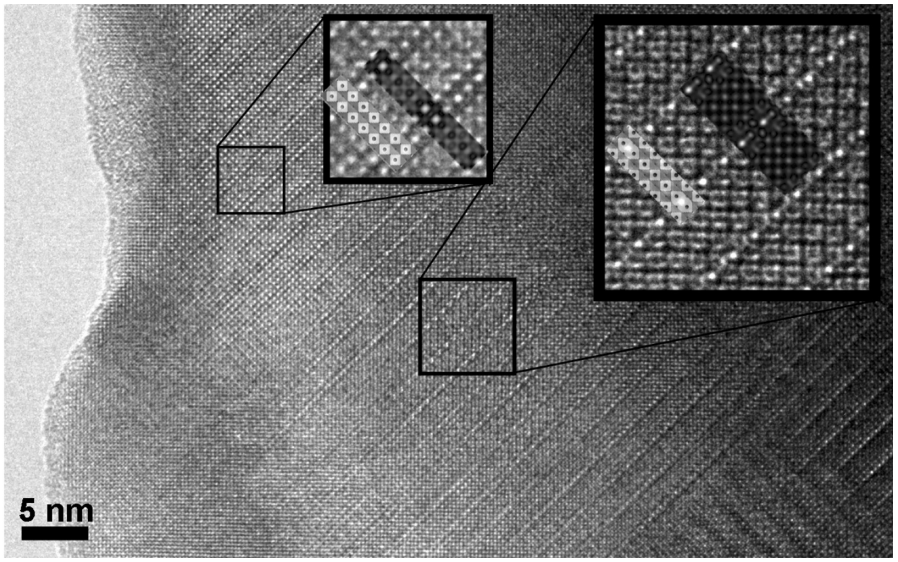

Figure 6. Shows a typical HRTEM image of a $\gamma = 0.40$ grain viewed near Scherzer defocus along an $\langle 001 \rangle_p$ projection direction. Twin domains corresponding to [010] and [100] domain orientations and typically 10−30 nm wide are visible. The insets show enlargements of these [010] and [100] twin domains, along with corresponding image simulations of the structure model shown in Figure 8d. Note the expected 5**x** repeat along the parent $\mathbf{c}_p$ direction on both the left and right hand sides of the image. On the right hand side of the image, corresponding to a [100] orientation, the repeat along the orthogonal $\mathbf{b}_p$ direction is clearly doubled, but this is not the case on the left hand side of the image which corresponds to an [010] orientation.

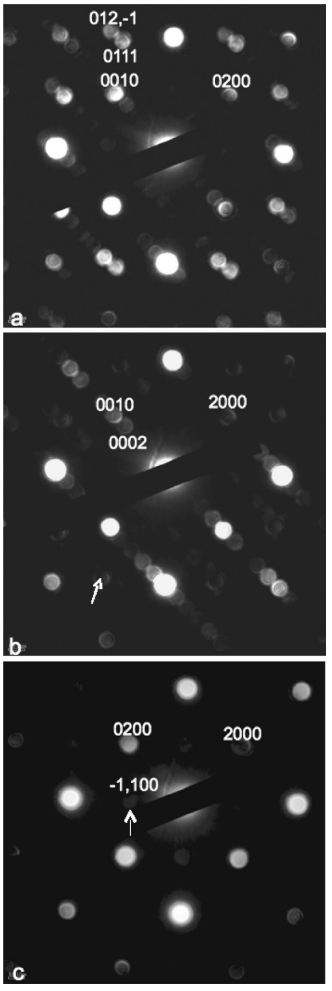

Figure 7. Shows (a) [100], (b) [010], and (c) [001] convergent beam patterns (CBPs) using a 2 nm diameter focused probe. Indexation is again with respect to the (3+1)-D reciprocal lattice basis vector set $M^* = \{{}^1/_2\ \mathbf{a}_p^*, {}^1/_2\ \mathbf{b}_p^*, \mathbf{c}_p^*, \mathbf{q} = \gamma \mathbf{c}_p^*\}$.

were much less well-defined than those in the BCFO samples, indicating that the BCFO samples order much more rapidly than the BSFO samples. This behavior is not unexpected, as the smaller size of the Ca^{2+} cations is likely to introduce significant local strain and thus force the BCFO to order more rapidly.

Figure 8 shows a [100] projection of various model structures for $\gamma = {}^2/_5$, corresponding to a 5**x** superstructure along $\mathbf{c}_p$ and to the HRTEM image shown on the right hand side of Figure 6. Figure 8a shows the model predicted in our previous paper[7] using a superspace approach. While this model has the correct number of vacancies and Bi/Ca ions, it could not be matched to the observed HRTEM images. An alternative model, shown in Figure 8b, was therefore developed. The arrows in Figure 8a show the shift in the position of a particular oxygen ion required to transform the oxygen/vacancy distribution shown in Figure 8a into that shown in Figure 8b. Note that tetrahedral as well as square pyramidal and octahedral coordination polyhedra are thereby created. This is unavoidable to maintain the overall stoichiometry but is also consistent with the Mössbauer results we have reported above. Note also that the Bi/Ca distribution also changes from Figure 8a to Figure 8b. Figure 8c corresponds to a symmetry equivalent version of Figure 8b. Figure 8d corresponds to an averaged version of Figure 8b,c. The oxygen ions shown in green are thus each half-occupied in Figure 8d. This is the model that was used to match to the experimental HRTEM images in Figure 6.

HRTEM images were simulated using this structure model. As shown in Figure 6, good agreement was obtained for both the [010] domain (on the left hand-side of the image) as well as the [100] domain (on the right hand-side of the image). In particular, in the [100] domain the oxygen vacancies are clearly imaged as single rows of bright white

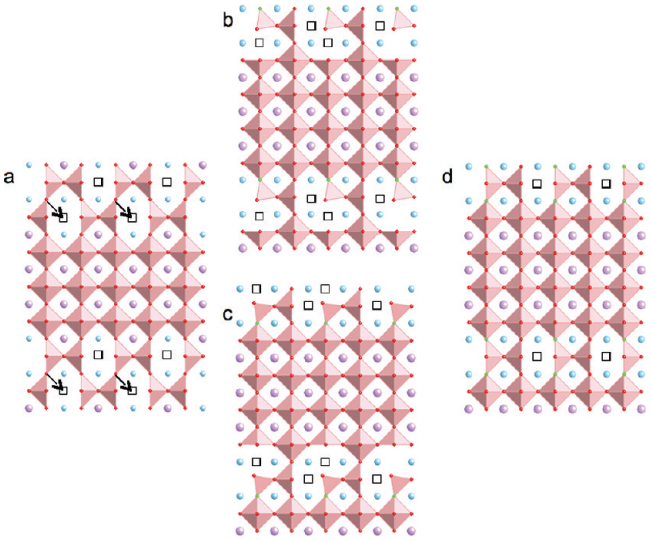

Figure 8. [100] projections of various models for $\gamma = 2/5$, corresponding to a 5**x** superstructure along c_p and to the HRTEM image shown in Figure 6. (a) Model predicted for $\gamma = 2/5$ from Withers et al.[7] An alternative structural model developed to fit the HRTEM image in Figure 6 is shown in (b). The arrows in (a) show the shift in the position of a particular oxygen ion required to transform the oxygen/vacancy distribution shown in (a) into (b). The FeO_4 tetrahedra, FeO_5 square pyramids and FeO_6 octahedra are shown in pink. The larger purple balls represent the Bi ions and the smaller blue balls represent the Ca ions, while the smallest red balls represent fully occupied oxygen ions. (c) corresponds to a symmetry equivalent version of (b). (d) corresponds to an averaged version of (b) and (c). The oxygen ions shown in green are each half-occupied in (d).

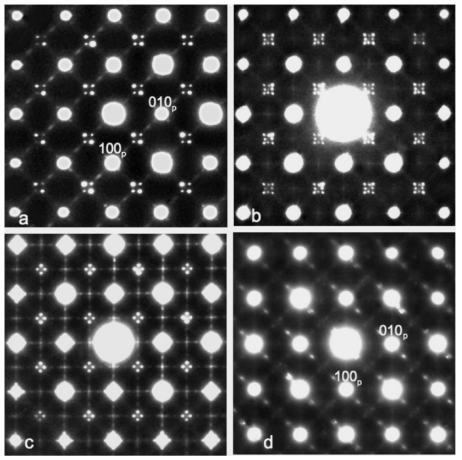

Figure 9. $\langle 001 \rangle_p$ zone axis EDPs of (a) an incommensurately modulated third phase found in the $x = 0.1$ sample, (c) the end-member $Bi_{1-x}Ca_xFeO_{3-x/2}$, $x \sim 0.2$, phase, (b) a composite EDP commonly found in the $x = 0.15$ sample, and (d) an unknown fourth phase found in a few grains of the $x = 0.1$ sample.

dots every $2b_P$ (cf. with Figure 8d). The smaller white dots in the image then correspond to the Fe and Bi cations. In the [010] domain region, the dominant features in the image are white dots corresponding to Bi and Ca cations and darker lines on both sides of the Ca−O vacancy block. A more detailed HRTEM investigation is underway to refine this structure model, particularly with regard to the oxygen-deficient region.

While the dominant phases observed in the $x = 0.1$ sample were the end-members of the compositionally

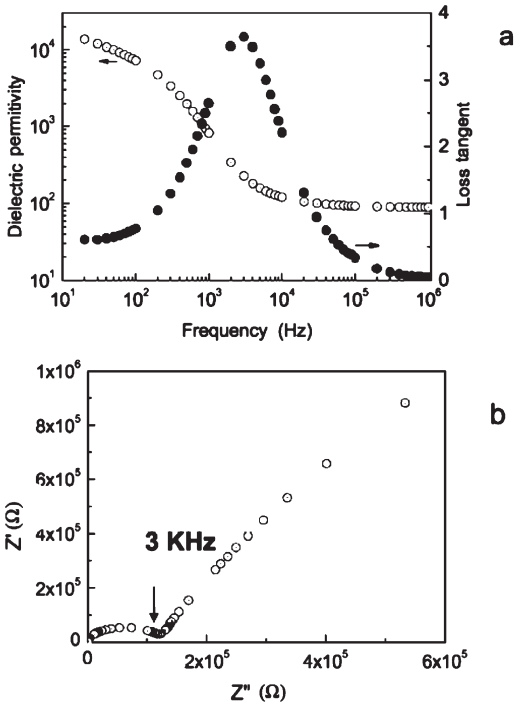

Figure 10. (a) Dielectric constant and loss tangent at room temperature for BCFO, $x = 0.36$, and (b) Cole−Cole plot of complex impedance for BCFO, $x = 0.36$.

narrow rhombohedral *R*3*c*, $Bi_{1-x}Ca_xFeO_{3-x/2}$, $0 < x < \sim 0.07$[9,10], and $Bi_{1-x}Ca_xFeO_{3-x/2}$, $\sim 0.2 < x < \sim 0.49$, solid solution phases, a third phase was observed in the $x = 0.1$ phase (see, e.g., the $\langle 001 \rangle_p$ EDP shown in Figure 9a). This phase is also incommensurately modulated but is distinguished from the $Bi_{1-x}Ca_xFeO_{3-x/2}$, $\sim 0.2 < x < \sim 0.49$, solid solution phase by the fact that the incommensurate modulation wave-vector runs along the $\langle 110 \rangle_p^*$ rather than the $\langle 001 \rangle_p^*$ direction. An untwinned version of this EDP has also recently been reported in Chen et al.[8] (see Figure 6b therein). This phase is likely to correspond to the second pseudo-tetragonal phase reported in Yang et al.[18] The same phase was also found in the $x = 0.15$ sample (see Figure 9b), but this time it was always intimately intergrown with the $x \sim 0.2$ end-member of the $Bi_{1-x}Ca_xFeO_{3-x/2}$, $\sim 0.2 < x < \sim 0.49$, solid solution phase (shown down the same orientation in Figure 9c); that is, Figure 9b is a composite of Figure 9a,c. Finally, a fourth phase showing $\mathbf{G} \pm \sim 1/4\langle 110 \rangle_p^*$ satellite reflections was also found in a few grains in the $x = 0.1$ sample but not in the $x = 0.15$ sample.

Electrical Characterization. Resistance measurements of the $x = 0.36$ sample (density > 92%) as a function of temperature showed semiconductor-like behavior. The measured resistivity was $\sim 10^{10}$ Ω·cm at −50°C, $\sim 10^5$ Ω·cm at room temperature, and only ~10 Ω·cm at 300 °C. Figure 10a shows the measured room temperature dielectric permittivity and loss tangent of this same sample as a function of applied frequency. At 1 MHz, the dielectric permittivity is 90 while the loss tangent is 0.04. Note that the dielectric permittivity decreases relatively sharply from $\sim 10^4$ to $\sim 10^2$ in the kHz region, becoming flat above 10^4 Hz. At the same time there is

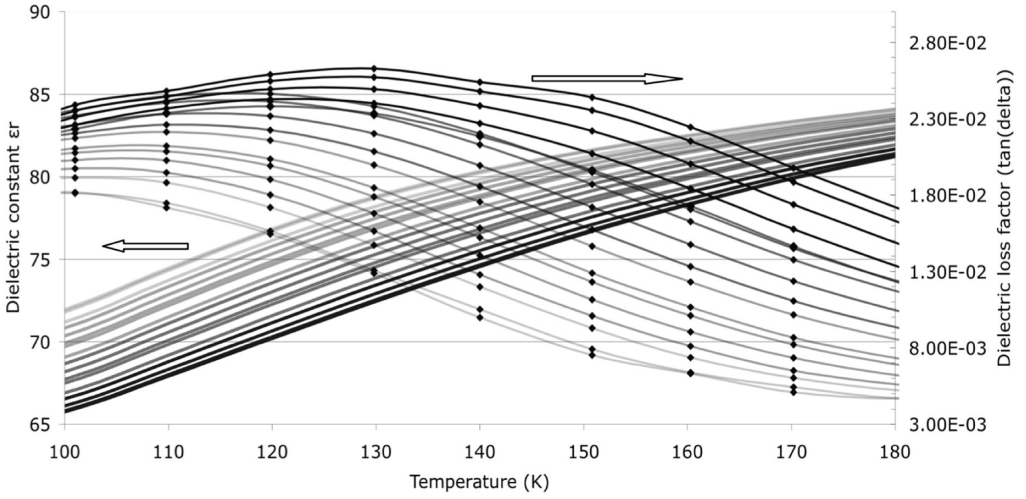

Figure 11. Dielectric constant and loss tangent between 100 and 180 K for BCFO, $x = 0.36$. The unmarked lines indicate the dielectric constant, while the diamond-marked lines indicate the dielectric loss tangent. Frequency is shown through shading, with line opacity increasing with increasing frequency from 800 Hz to 1 MHz. The frequencies shown are (in Hz): 800, 1k, 2k, 3k, 4k, 5k, 8k, 10k, 20k, 30k, 50k, 80k, 100k, 200k, 300k, 500k, 800k, and 1 MHz.

an accompanying peak in the dielectric loss tangent at ~3 kHz. The complex impedance was thus measured (Figure 10b) to better understand the corresponding polarization relaxation mechanism. The resultant Cole−Cole plot includes two parts: a semi-circle on the left hand side of the figure and an approximately linear section on the right hand side of the figure. The linear increase in the real part of the impedance indicates a conductive mechanism in the low frequency range. The semicircle corresponds to polarization originating within grains. After the semicircle, the real part of the impedance increases continually from approximately 3 kHz. This frequency corresponds to the peak of the loss tangent shown in Figure 10a, suggesting that the observed relaxation is an intrinsic feature from within the sample grains.

To obtain more information as to the nature of the dielectric relaxation responsible, the dielectric permittivity and loss tangent were also measured at various frequencies as a function of temperature. Only one relaxation peak was observed at low temperature, as shown in Figure 11. Using the Arrhenius equation: $f = f_0 e^{-E_a/(kT_m)}$, the activation energy (E_a) and freezing frequency (f_0) of the dipoles were measured, based on the frequency at which the maximum in the loss tangent is observed at low temperature. The fitted plot is shown in Figure 12. The obtained freezing frequency and activation energy of the dipoles were 1.89×10^{14} Hz and 0.22 eV, respectively. According to the structural model proposed in Figure 8 above, the only possible source of intrinsic dynamic dipoles are those resulting either from oxygen vacancy hopping or from off-center displacements of the Bi/Ca ions. It is expected that the energy required to switch the off-center positions of the heavy cations and move any domain walls present would require a largeish activation energy (~1.3 eV in PZT, for

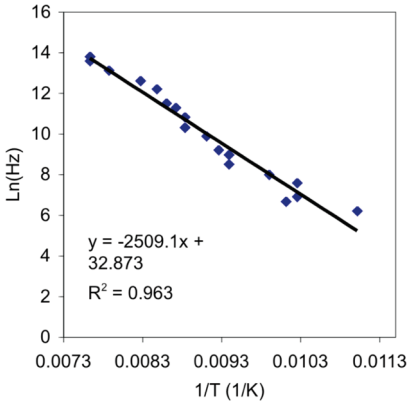

Figure 12. Log of frequency at which the dielectric loss is maximal against 1/temperature for BCFO, $x = 0.36$.

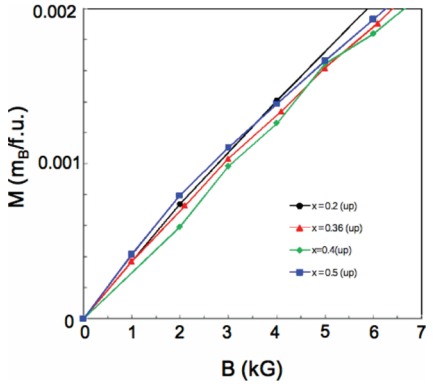

Figure 13. Magnetization per formula unit as a function of applied field for $x = 0.2$, 0.3, 0.36, 0.4 and 0.5.

example).[23] We thus suggest that the observed relaxation at low temperature (~100 K) be assigned to oxygen vacancy hopping. The calculated activation energy of 0.22 eV is consistent with previous investigations of oxygen vacancy hopping in related materials. While the binding energy of an isolated oxygen vacancy is ~0.60 eV, the binding energy of oxygen vacancy clusters (0.26 eV for

(23) Can, W.; Fang, Q. F.; Zhu, Z. G. *J. Phys. D: Appl. Phys.* **2002**, *13*, 1545.

a chain and 0.20 eV for a pair)[24] is rather close to the measured value of 0.22 eV. It is thus concluded that the observed dielectric relaxation originates from the hopping of oxygen vacancies between alternative sites in the double Ca layer shown in Figure 8.

Ferroelectric hysteresis loops could not be obtained at room temperature and zero magnetic field as a result of the intrinsic semiconductivity of the materials. This does not, however, preclude the existence of coordinated ferroic ion displacements. It may be expected that the behavior of this system under a magnetic field will be very similar to that reported for the strontium analogue phase, with magnetic field induced ferroelectric behavior.[9]

Magnetic Property Measurements. Finally, the room temperature magnetization was recorded as a function of applied field for five different BCFO samples. This data is presented in Figure 13 in Bohr magnetons/formula unit.

In each case, the data exhibit an approximately linear behavior with no significant spontaneous magnetization or irreversible effects. The magnetization of 0.088 emu g^{-1} recorded for $x = 0.3$ at 14 kOe is in excellent agreement with the recent work of Khomchenko et al.[20] The data recorded show almost identical magnetization for all samples up to 7 kG. This consistent magnetization indicates that there is no change in iron valence state throughout the solid solution range, as also supported by the Mössbauer results described above.

Acknowledgment. The ANU Electron Microscopy Unit are acknowledged for the use of SEM and TEM equipment and the provision of expert advice and training. J.S., R.L.W., and Y.L. thank the ARC for financial support in the form of ARC Discovery Grants.

(24) Cordero, F. *Phys. Rev. B: Condens. Matter Mater. Phys.* **2007**, *76* (17), 172106-4.